

Theoretically Optimal Attention/FFN Ratios in Disaggregated LLM Serving

Chendong Song¹ Meixuan Wang² Hang Zhou³ Hong Liang⁴ Yuan Lyu⁴ Zixi Chen⁵ Yuwei Fan⁴
Zijie Zhou¹

Abstract

Attention-FFN disaggregation (AFD) is an emerging architecture for LLM decoding that separates state-heavy, KV-cache-dominated Attention computation from stateless, compute-intensive FFN computation, connected by per-step communication. While AFD enables independent scaling of memory and compute resources, its performance is highly sensitive to the Attention/FFN provisioning ratio: mis-sizing induces step-level blocking and costly device idle time. We develop a tractable analytical framework for sizing AFD bundles in an $rA-1F$ topology, where the key difficulty is that Attention-side work is nonstationary—token context grows and requests are continuously replenished with random lengths—while FFN work is stable given the aggregated batch. Using a probabilistic workload model, we derive closed-form rules for the optimal A/F ratio that maximize average throughput per instance across the system. A trace-calibrated AFD simulator validates the theory: across workloads, the theoretical optimal A/F ratio matches the simulation-optimal within 10%, and consistently reduces idle time.

1. Introduction

The explosive growth of large language models (LLMs) (Brown et al., 2020; Chowdhery et al., 2023; OpenAI, 2023; Kaplan et al., 2020) has created unprecedented challenges for efficient inference serving at scale. As model sizes expand into hundreds of billions of parameters, modern LLM serving inevitably requires distributed multi-device archi-

tures. This reality has spurred a shift from monolithic serving paradigms toward increasingly sophisticated disaggregation strategies that decompose the inference pipeline across heterogeneous hardware resources.

Early efforts of disaggregate serving focused on stage-level separation, exemplified by the Prefill-Decode (PD) disaggregation (Zhong et al., 2024; Patel et al., 2024). LLM inference comprises two phases with distinct resource profiles: *prefill* processes the input prompt and generates the KV cache via dense matrix operations (compute-bound), while *decode* generates tokens autoregressively, reading the accumulated KV cache at each step (memory-bound). PD disaggregation separates these phases onto hardware matched to their respective bottlenecks. By disaggregating prefill and decode onto separate hardware pools that can be independently scaled, PD architectures enable higher decode batch sizes through request aggregation, improving GPU utilization during token generation.

Building upon this foundation, recent research has recognized that even within the decode phase, computational heterogeneity persists between different transformer components. The Attention-FFN Decoupling (AFD) (Wang et al., 2025; Zhang et al., 2025; Zhu et al., 2025; Zuo et al., 2025) extends this disaggregation further: Attention layers are stateful and memory-bound (dominated by KV cache reads), whereas FFN layers are stateless and can achieve compute-bound operation with sufficient batching. Traditional coupled architectures often leave FFN compute units underutilized due to the small decode batch with TPOT constraints. AFD architecture strategically disaggregates these components, allowing multiple Attention instances—which host the massive KV cache states—to feed into an aggregated FFN instances. This topology maximizes FFN arithmetic intensity while independently scaling memory resources for Attention.

Recent work (Wang et al., 2025; Zhu et al., 2025; Zuo et al., 2025) has shown that AFD can significantly improve serving efficiency by allowing Attention and FFN to scale independently. Given this flexibility, a central design decision in such systems is the ratio of Attention instances to FFN instances, which we denote as r . Currently, existing systems set r through empirical search, yet a theoretical foundation

¹Department of Industrial Engineering and Decision Analytics, HKUST, Clear Water Bay, Hongkong, China ²Department of Computer Science and Technology, Tsinghua University, Haidian District, 100084, Beijing, China ³Institute for Interdisciplinary Information Sciences, Tsinghua University, Haidian District, 100084, Beijing, China ⁴Huawei Hong Kong Research Center, Hong Kong, China. ⁵School of Mathematical Sciences, Peking University, Yihuyuan Road, 100871, Beijing, China. Correspondence to: Chendong Song <songcd@ust.hk>, Zijie Zhou <jerryzhou@ust.hk>.

for optimal sizing is still lacking. This gap matters because the choice of r directly impacts system efficiency—when r is too small, the FFN server starves for input; when r is too large, Attention instances block waiting for FFN availability.

Finding the optimal r , however, is non-trivial. The key difficulty is that Attention and FFN workloads scale differently. FFN computation depends only on batch size and remains stable across decode steps. In contrast, Attention workload evolves continuously—the KV cache grows with each step, and completed requests are replaced by new ones with variable prompt lengths.

As AFD remains an emerging paradigm with no mature open-source implementations, principled **theoretical foundations** are needed to guide this design space before extensive system building begins. In this paper, we provide such foundations through a rigorous probabilistic framework that captures the stochastic dynamics of Attention-side workload and derives a closed-form expression for the optimal A/F ratio. Our simulation-based validation demonstrates that the theory accurately predicts system behavior; real-system validation is left to future work as AFD implementations mature. Our contributions are summarized as follows:

- **Probabilistic workload model.** We develop a rigorous analytical framework that captures the real dynamics of AFD serving, including microbatch pipelining, synchronization barriers, and continuous batching with request replenishment. By tracking the non-stationary evolution of per-slot KV cache loads across decode steps, we derive the horizon-average token load, which accurately characterizes the time-varying Attention computation cost.
- **Closed-form optimal A/F ratio.** We derive an analytical expression for the optimal Attention-to-FFN ratio r^* and characterize three operating regimes (Attention-bottleneck, Communication-bottleneck, and FFN-bottleneck), each with interpretable optimality conditions.
- **Simulation validation.** We develop an AFD simulator and conduct extensive experiments across diverse workload configurations. The theoretical optimal A/F ratio match simulation results within 10% relative error, and ablation studies reveal that the optimal A/F ratio increases with both batch size and context length.

2. Background on Attention-FFN Disaggregation: Pipeline and Microbatch

In standard LLM decoding, a monolithic architecture deploys both Attention and FFN blocks on the same hardware. To reduce kernel launch overhead and execution bubbles,

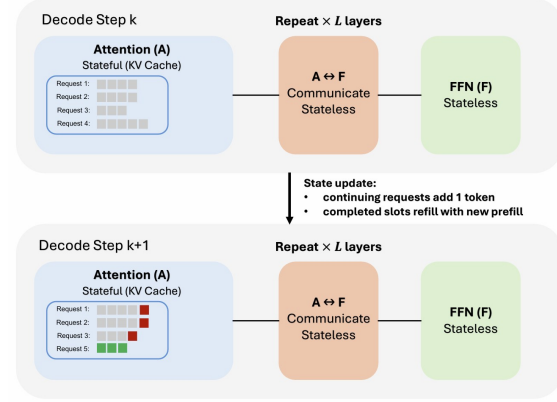


Figure 1. Architecture of AFD. Stateful Attention (A) layers manage the KV cache, while Feed-Forward Network (F) layers are stateless. During each decode step, every continuing request generates one output token whose key-value is appended to the KV cache (red blocks); when a request completes, its slot is immediately refilled with a new prefill request (green block).

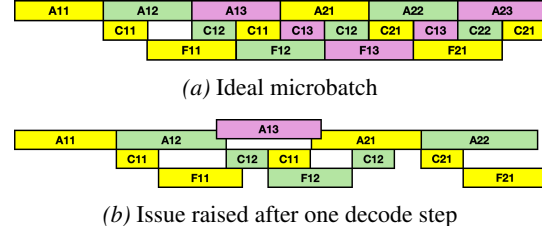


Figure 2. Microbatch Pipelining and Masking. (a) An ideal schedule where Attention, Communication, and FFN are perfectly overlapped across microbatches, fully hiding data transfer latency. (b) After one decode step, Attention execution time increases (due to longer KV cache reads) while Communication and FFN remain unchanged, breaking the balanced overlap and introducing pipeline bubbles.

practitioners typically compile the model into a static execution graph (e.g., CUDA Graphs (Ekelund et al., 2025)), which enforces fixed batch sizes across all components. This rigidity creates a utilization problem: time per output token (TPOT) latency constraints force small batch sizes, and at low concurrency, FFN blocks cannot amortize their weight-loading cost—despite being computationally dense, they become memory-bandwidth bound rather than compute-bound.

AFD addresses this by disaggregating Attention and FFN onto separate hardware, enabling an asymmetric $r : 1$ deployment where multiple Attention instances feed a shared FFN server. We now describe the execution mechanics of this architecture.

In an AF-disaggregated deployment, each Transformer layer comprises three distinct stages: Attention computation, FFN computation, and inter-device Communication ($A \leftrightarrow F$). As illustrated in Figure 1, Attention blocks are stateful: dur-

ing each decode step, every continuing request generates one output token, and its corresponding key-value is appended to the KV cache. When computing attention, the model must read the entire accumulated KV cache for each request, so the Attention cost grows linearly with sequence length. When a request completes, its slot is immediately refilled with a new prefill request to maintain batch size (continuous batching). In contrast, FFN blocks are stateless—their computation depends only on the current activations, not on sequence history. To handle the latency introduced by transferring activations (AF communication) across L layers within one decode step, microbatch pipelining is adopted, as shown in Figure 2.

Figure 2(a) depicts an ideal execution schedule. Here, A_{mn} , C_{mn} , and F_{mn} denote Attention, Communication, and FFN operations for the n -th microbatch at the m -th layer, respectively. With sufficient microbatches (typically ≥ 3), the system overlaps Communication and FFN of one microbatch with Attention of subsequent microbatches, thereby masking data transfer (communication) latency.

However, Attention’s stateful nature introduces dynamic variability that disrupts this ideal schedule. Consider Figure 2(b): after one decode step, assuming no request completes, every request’s KV cache has grown by one token. Consequently, A_{11} , A_{12} , and A_{13} all take longer than in the previous step, while C_{mn} and F_{mn} remain unchanged. The increased Attention time means that A_{12} and A_{13} can no longer fit in the gaps between layers— A_{13} is deferred, leaving idle “bubbles” in the pipeline. Depending on the workload imbalance, bubbles may appear on the Attention side (waiting for FFN) or the FFN side (starved of data from Attention). Since Attention workload drifts continuously, no static microbatch schedule remains ideal over time. This motivates our central question: how to determine the optimal Attention-to-FFN ratio ($r:1$) that minimizes expected pipeline bubbles across a long serving horizon.

3. Mathematical Model

We formalize the AFD serving system and define our optimization objective. Table 1 summarizes key notation.

Table 1. Key notations.

Symbol	Description
r	Number of Attention instances per FFN instance
B	Microbatch size per Attention instance
T	Total token load (sum of KV cache lengths)
$\tau(B; r)$	Per-step cycle time
μ_P	Mean prefill length
μ_D	Mean decode length
p	Per-step termination probability

3.1. AFD Bundle Architecture

We consider an AFD bundle in a general $xA-yF$ topology, where x Attention instances feed into y shared FFN instances. To simplify notation, we define the Attention-to-FFN ratio $r := x/y$ and express the topology equivalently as $rA-1F$. r does not need to be an integer, for example, $r = 3.5$ corresponds to a 7A-2F configuration. Each Attention instance maintains a microbatch of B requests and their associated KV caches. Decoding proceeds in synchronized steps, where each step comprises four phases:

- (i) *Attention phase*: The r Attention workers execute in parallel, each processing its microbatch of B requests (total rB requests across the bundle).
- (ii) *A→F communication*: All r Attention workers transfer their intermediate activations to the shared FFN worker.
- (iii) *FFN phase*: The FFN worker processes the aggregated batch of rB activations.
- (iv) *F→A communication*: The FFN worker returns outputs to all r Attention workers.

Our goal is to determine the optimal ratio r^* that maximizes system throughput.

3.2. Latency Models

We adopt linear latency models grounded in first-principles hardware analysis (see Appendix B for detailed derivations) and consistent with established results in the LLM inference literature.

Attention. The Attention computation reads the KV cache for all requests in the microbatch. For a microbatch of B requests, let s_b denote the prefill length and i_b the current decode index (number of tokens generated so far) for request b . The total token load is

$$T = \sum_{b=1}^B (s_b + i_b). \quad (1)$$

During decoding, the Attention computation is memory-bandwidth bound-dominated by reading the KV cache from HBM (Kwon et al., 2023; Pope et al., 2023; Agrawal et al., 2024). The latency scales linearly with the total token load T :

$$t_A(T) = \alpha_A T + \beta_A. \quad (2)$$

This linear relationship follows directly from the roofline model: when an operation is memory-bound, latency equals data volume divided by effective bandwidth (Yuan et al., 2024; Lienhart, 2024). Since each token requires reading a fixed number of bytes from the KV cache, Attention latency

grows linearly with sequence length (NVIDIA, 2023; Dao et al., 2022).

FFN. The FFN processes batched activations and becomes compute-bound with sufficient batching (Agrawal et al., 2024; Wei et al., 2024). The latency scales linearly with batch size:

$$t_F(rB) = \alpha_F(rB) + \beta_F. \quad (3)$$

This linear scaling is well-established: FFN layers perform matrix multiplications where FLOPs scale as $O(\text{batch size} \times \text{hidden dimension} \times \text{expert intermediate size})$, yielding linear latency when compute-bound (Pope et al., 2023; Chen, 2023).

Communication. The round-trip communication cost per Attention instance is

$$t_C(B) = \alpha_C B + \beta_C. \quad (4)$$

This linear model, where latency comprises a fixed startup cost β_C plus a bandwidth-dependent term proportional to data volume $\alpha_C B$, is the foundational model for distributed communication and has been validated extensively in GPU clusters (Narayanan et al., 2021; Li et al., 2024).

3.3. Workload Characterization

Request lengths. Each request has a prefill length P (input prompt tokens) and decode length D (output tokens to generate). We model:

- **Prefill:** P follows a bounded distribution with mean μ_P . Our analysis requires only the mean; the specific distribution does not affect the results.
- **Decode:** Empirical analysis of LLM serving traces reveals that decode lengths closely follow a geometric distribution (discrete-exponential) (Figure 3). We model $D \sim \text{Geo}(p)$ on $\{0, 1, 2, \dots\}$, where p is the per-step termination probability, giving mean $\mu_D = (1 - p)/p$.

The geometric model for decode lengths is not merely convenient—it reflects the autoregressive nature of LLM generation, where at each step the model may produce an end-of-sequence token with roughly constant probability, independent of how many tokens have been generated. This *memoryless property* is key to our tractable analysis.

Continuous batching. Following standard practice in LLM serving, we use continuous batching: whenever a request completes, its slot is immediately refilled with a new request from the queue. This maintains full microbatches throughout serving.

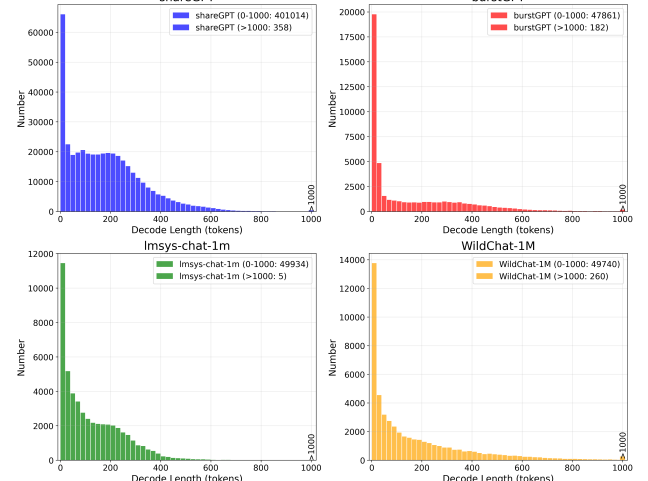


Figure 3. Empirical distributions of decode lengths from production LLM traces (Wang et al., 2023; 2024; Zheng et al., 2023; Zhao et al., 2024). Decode lengths exhibit a geometric (discrete-exponential) pattern.

3.4. Optimization Objective

Cycle time. The per-step cycle time is determined by the slowest component:

$$\tau(B; r) = \max \{t_A(T), t_C(B), t_F(rB)\}. \quad (5)$$

Throughput per instance. We maximize the average number of output tokens generated per unit time, normalized by the total number of instances (r Attention + 1 FFN):

$$\text{Throughput}_{\text{per-inst}}(B; r) = \frac{1}{r+1} \cdot \frac{rB}{\tau(B; r)}, \quad (6)$$

where rB is the number of tokens generated per cycle across the bundle.

The central challenge is that T in (5) is *non-stationary*: it evolves as decoding progresses and requests are replaced. The next section develops a probabilistic analysis to characterize this dynamic workload.

4. Analysis and Optimal A/F Ratio

We now derive the optimal Attention-to-FFN ratio r^* . We first analyze the stochastic dynamics of Attention workload, derive a closed-form approximation for the horizon-average token load, and then characterize the optimal ratio across different operating regimes.

4.1. Token-Load Dynamics

By symmetry, it suffices to analyze one representative Attention instance. At decode step $k \in \{0, 1, 2, \dots\}$, let $i_b(k)$ be the decode index of slot $b \in \{1, \dots, B\}$, and let $s_b(k)$

be the prefill length of the request currently occupying that slot. Define the aggregate quantities:

$$D_k := \sum_{b=1}^B i_b(k), \quad P_k := \sum_{b=1}^B s_b(k), \quad T_k := P_k + D_k.$$

Update dynamics. Let $X_b(k) \sim \text{Bernoulli}(1 - p)$ indicate whether slot b continues (does not complete) at step k . The decode index updates as:

$$i_b(k+1) = X_b(k) \cdot (i_b(k) + 1). \quad (7)$$

If the request continues, its decode index increments; if it completes, the slot is refilled with a new request starting at $i_b(k+1) = 0$.

For prefill, the slot retains its prefill length if continuing, or draws a fresh value upon replacement:

$$s_b(k+1) = X_b(k) \cdot s_b(k) + (1 - X_b(k)) \cdot S'_b(k), \quad (8)$$

where $S'_b(k)$ is the prefill length of the incoming request, with $\mathbb{E}[S'_b(k)] = \mu_P$.

Key insight: memoryless dynamics. The geometric distribution's memoryless property ensures that $X_b(k)$ is *independent* of $i_b(k)$ —at any step, regardless of how long a request has been running, it terminates with probability p . This independence yields clean Markovian dynamics that admit closed-form analysis.

Lemma 4.1 (Expected token load). *Under the dynamics (7)–(8):*

$$\mathbb{E}[P_k] = B\mu_P, \quad \forall k \geq 0, \quad (9)$$

$$\mathbb{E}[D_k] = B \frac{1-p}{p} \left(1 - (1-p)^k\right), \quad \forall k \geq 0, \quad (10)$$

and thus

$$\mathbb{E}[T_k] = B\mu_P + B \frac{1-p}{p} \left(1 - (1-p)^k\right). \quad (11)$$

Proof sketch. For (9): Taking expectations in (8) and using $\mathbb{E}[S'_b(k)] = \mu_P$ yields a recursion whose unique fixed point is $\mathbb{E}[P_k] = B\mu_P$.

For (10): From (7), $\mathbb{E}[D_{k+1}] = (1-p)(\mathbb{E}[D_k] + B)$. Solving this recursion with $D_0 = 0$ gives (10). The full proof is in Appendix A. \square

Lemma 4.1 reveals that the expected prefill load is constant, while the expected decode load grows from zero and saturates at $B(1-p)/p = B\mu_D$ as $k \rightarrow \infty$.

4.2. Horizon-Average Token Load

To obtain a representative Attention workload for optimization, we average $\mathbb{E}[T_k]$ over the serving horizon.

Let N be the total number of requests served by one Attention instance. Since each step completes an expected Bp requests, the expected number of steps is

$$K(B) = \frac{N}{Bp}. \quad (12)$$

Definition 4.2 (Horizon-average token load).

$$\bar{T}(B; N) := \frac{1}{K(B)} \sum_{k=0}^{K(B)-1} \mathbb{E}[T_k]. \quad (13)$$

Proposition 4.3 (Law of Large Numbers). *For large N :*

$$\bar{T} = \lim_{N \rightarrow \infty} \bar{T}(B; N) = \left(\mu_P + \frac{1-p}{p} \right) B, \quad (14)$$

The proof can be found in Appendix A, which sums the geometric series in (11) over the horizon.

4.3. Regime Analysis

Substituting \bar{T} from (14) into the cycle time (5), we can analyze how throughput varies with r . Let

$$\bar{t}_A := \alpha_A \bar{T} + \beta_A, \quad \bar{t}_C := \alpha_C B + \beta_C, \quad \bar{t}_F(r) := \alpha_F r B + \beta_F.$$

Define the dominant non-FFN latency:

$$M(B) := \max\{\bar{t}_A, \bar{t}_C\}.$$

The structure of $\tau(B; r) = \max\{\bar{t}_A, \bar{t}_C, \bar{t}_F(r)\}$ partitions the feasible region into three regimes.

4.3.1. REGIME I: ATTENTION-BOTTLENECK

Condition: $\bar{t}_A \geq \bar{t}_C$ and $\bar{t}_A \geq \bar{t}_F(r)$, i.e., $r \leq r_A$ where

$$r_A := \frac{\bar{t}_A - \beta_F}{\alpha_F B}. \quad (15)$$

Analysis: The cycle time is pinned at \bar{t}_A , independent of r . Throughput becomes

$$\text{Throughput}_{\text{per-inst}}(r) = \frac{B}{\bar{t}_A} \cdot \frac{r}{r+1},$$

which is strictly increasing in r . The optimum within this regime is at the boundary: $r_1^* = r_A$.

4.3.2. REGIME II: COMMUNICATION-BOTTLENECK

Condition: $\bar{t}_C \geq \bar{t}_A$ and $\bar{t}_C \geq \bar{t}_F(r)$, i.e., $r \leq r_C$ where

$$r_C := \frac{\bar{t}_C - \beta_F}{\alpha_F B}. \quad (16)$$

Analysis: The cycle time is pinned at \bar{t}_C . By identical reasoning, throughput is increasing in r , and the regime optimum is $r_{II}^* = r_C$.

4.3.3. REGIME III: FFN-BOTTLENECK

Condition: $\bar{t}_F(r) \geq M(B)$, i.e., $r \geq r_{\text{crit}}$ where

$$r_{\text{crit}} := \frac{M(B) - \beta_F}{\alpha_F B}. \quad (17)$$

Analysis: The cycle time grows with r , creating a trade-off: larger r increases the numerator rB in (6) but also increases τ . The throughput is

$$f(r) := \frac{rB}{(r+1)(\alpha_F r B + \beta_F)}.$$

Setting $f'(r) = 0$ yields the unconstrained maximizer:

$$r_{\text{peak}} = \sqrt{\frac{\beta_F}{\alpha_F B}}. \quad (18)$$

Since $f(r)$ is unimodal (increasing for $r < r_{\text{peak}}$, decreasing for $r > r_{\text{peak}}$), the constrained optimum in Regime III is

$$r_{III}^* = \max\{r_{\text{crit}}, r_{\text{peak}}\}.$$

4.4. Optimal Ratio

Combining the regime analysis yields our main result.

Theorem 4.4 (Optimal A/F Ratio). *The globally optimal A/F ratio is*

$$r^* = \max \left\{ \frac{\alpha_A \bar{T} + \beta_A - \beta_F}{\alpha_F B}, \frac{\bar{t}_C - \beta_F}{\alpha_F B}, \sqrt{\frac{\beta_F}{\alpha_F B}} \right\} \quad (19)$$

with corresponding throughput

$$\text{Throughput}^* = \frac{r^* B}{(r^* + 1)(\alpha_F r^* B + \beta_F)}. \quad (20)$$

Interpretation. The optimal ratio is the maximum of three terms:

- $r_A = (\alpha_A \bar{T} + \beta_A - \beta_F)/(\alpha_F B)$: the *balance point* where Attention and FFN latencies are equal. Operating below this wastes FFN capacity.

- $r_C = \frac{\bar{t}_C - \beta_F}{\alpha_F B}$: the communication dominates the process, but this is typically rare in practice.
- $r_{\text{peak}} = \sqrt{\beta_F/(\alpha_F B)}$: the *throughput peak* in the FFN-bottleneck regime, arising from the trade-off between batch aggregation and FFN congestion.

Practical recipe. Given hardware parameters $(\alpha_A, \beta_A, \alpha_F, \beta_F)$ and workload statistics (μ_P, μ_D) :

1. Compute $\bar{T} \approx B(\mu_P + \mu_D)$ for large N .
2. Compute r_A, r_C and r_{peak} from (15), (16), and (18), respectively.
3. Set $r^* = \max\{r_A, r_C, r_{\text{peak}}\}$.

5. Numerical Experiments

To validate our theoretical framework, we develop an AFD simulator and conduct systematic experiments comparing theoretical predictions with simulation results. The source code is available at <https://anonymous.4open.science/r/AF-release-1C11>.

5.1. Simulator Design

The simulator implements a discrete-event, cycle-by-cycle simulation of the rA-1F topology, where each Batch object transitions through a six-state finite state machine (Attention \rightarrow A2F transfer \rightarrow Waiting \rightarrow FFN \rightarrow F2A transfer \rightarrow Waiting \rightarrow repeat). To maximize resource utilization, the simulator maintains two batches in flight simultaneously: while one batch is being processed by the shared FFN server, the Attention instances process the other batch in parallel, and vice versa. This interleaved execution allows computation on one batch to overlap with communication and processing of the other, effectively hiding transfer latencies.

The simulator enforces continuous batching (Kwon et al., 2023) by maintaining a global FCFS buffer. Whenever a request completes within a batch, the vacated slot is immediately refilled from the buffer before the next decode step begins, ensuring that each Attention instance consistently processes a full microbatch of size B .

5.2. Experimental Setup

Latency Parameters. We adopt the linear coefficients with parameters calibrated for the DeepSeek-V3 architecture deployed on Huawei Ascend 910C NPUs. The coefficients are obtained via linear regression on real execution traces collected from the deployment, which can be found in Table 2. Appendix B provides the general derivation framework, enabling practitioners to calibrate these parameters for other hardware platforms.

Table 2. Latency parameters

Parameter	Symbol	Value	Description
Attention slope	α_A	0.00165	cycles/token
Attention intercept	β_A	50	cycles
FFN slope	α_F	0.083	cycles/request
FFN intercept	β_F	100	cycles
Comm slope	α_C	0.022	cycles/token
Comm intercept	β_C	20	cycles

Under this configuration, communication latency can be effectively hidden through pipelining. Specifically, both t_A and t_F exceed $2 \times t_C$ across operating regimes. Consequently, our analysis focuses on balancing Attention and FFN workloads as the primary optimization target.

Evaluation Metrics. We evaluate the following metrics to assess system performance:

- **Stable Throughput per Instance** To avoid distortion from startup transients and tail effects (e.g., the final requests draining with partially filled batches), we report throughput computed over the first 80% of completed requests. Specifically, we measure $T_{80\%}$ as the time when $\lceil 0.8N \rceil$ requests have completed, and compute

$$\text{Throughput}_{\text{per-inst}}^{(80\%)} = \frac{1}{r+1} \cdot \frac{\sum_{i=1}^{\lceil 0.8N \rceil} D_i}{T_{80\%}}, \quad (21)$$

where D_i is the number of output tokens generated for the i -th request. This approach ensures that our measurements reflect stable performance rather than boundary artifacts.

- **Time Per Output Token (TPOT):** The average time to generate a single output token per request, defined as

$$\text{TPOT} = \frac{1}{N} \sum_{i=1}^N \frac{T_{\text{decode}}^{(i)}}{D_i}, \quad (22)$$

where $T_{\text{decode}}^{(i)}$ denotes the total decode time (from the first output token to completion) for the i -th request.

- **Idle Ratios:** To quantify resource utilization, we measure the fraction of time that each component remains idle waiting for synchronization:

$$\eta_A = \frac{1}{r} \sum_{i=1}^r \frac{t_{\text{idle},A}^{(i)}}{T_{\text{total}}}, \quad \eta_F = \frac{t_{\text{idle},F}}{T_{\text{total}}}, \quad (23)$$

where $t_{\text{idle},A}^{(i)}$ and $t_{\text{idle},F}$ denote the total idle waiting time of the i -th Attention instance and the shared FFN instance, respectively. Lower values indicate better utilization; in an ideally balanced system, both $\eta_A, \eta_F \rightarrow 0$.

5.3. Results

We first study how the Attention-to-FFN ratio r affects throughput and resource utilization under our baseline configuration.

Setup. We fix batch size $B = 256$, expected decode length $\mu_D = 500$ tokens, and expected prefill length $\mu_P = 100$ tokens. We sweep $r \in \{1, 2, 4, 8, 16, 24, 32\}$ and simulate until $N = 10,000$ requests complete per Attention instance. In this setting, we can calculate the optimal theoretical A/F ratio:

$$r_{\text{theory}}^* = \max \left\{ \frac{\alpha_A \bar{T} + \beta_A - \beta_F}{\alpha_F B}, \sqrt{\frac{\beta_F}{\alpha_F B}} \right\} \approx 9.3.$$

Results. Figure 4 shows per-instance throughput as a function of r . The theoretical optimal $r_{\text{theory}}^* \approx 9.3$ closely matches the simulation-optimal ratio. Moreover, the theoretical throughput curve tracks the simulation results well across all configurations, validating our analytical framework.

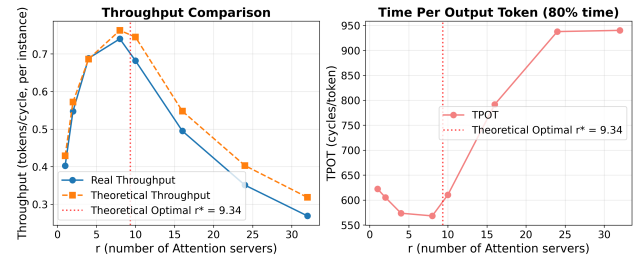


Figure 4. Per-instance throughput as a function of A/F ratio r with $B = 256$, $\mu_D = 500$, $\mu_P = 100$. Throughput increases with r until reaching the optimal point $r^* \approx 9.3$, after which FFN becomes saturated and throughput per instance decreases.

We notice a systematic gap emerges at large r : simulated throughput falls increasingly below the theoretical prediction, with the discrepancy reaching approximately 15% at $r = 32$. This gap arises from inherent load imbalance across Attention instances. Stochastic request dynamics create heterogeneous token loads, and since all r instances must synchronize before the FFN phase, the system waits for the slowest instance at each step—with straggler probability growing as r increases. Implementing load-balancing strategies (Chen et al., 2026) can mitigate this gap, though some irreducible variance from stochastic dynamics remains.

Figure 5 presents the idle ratios for Attention (η_A) and FFN (η_F) instances. When r is small, FFN completes quickly and idles while waiting for Attention outputs ($\eta_F > 60\%$ at $r = 1$). As r increases, more Attention instances feed the shared FFN, improving its utilization. Conversely, when r is large, FFN becomes saturated and Attention instances must wait ($\eta_A > 60\%$ at $r = 32$).

The crossover point (At around $r = 8$) where $\eta_A \approx \eta_F$ corresponds to the balanced configuration that maximizes throughput, confirming that our theoretical framework correctly identifies the optimal operating regime.

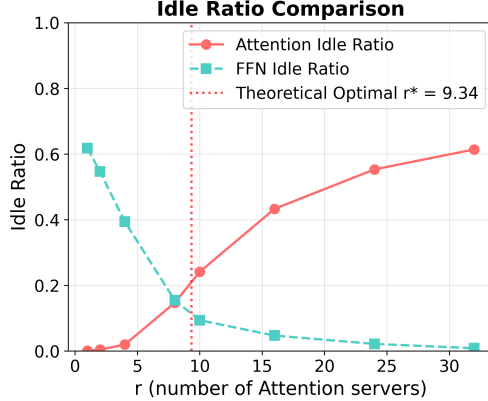


Figure 5. Attention idle ratio η_A (blue) and FFN idle ratio η_F (orange) as functions of A/F ratio r . The crossover point where $\eta_A \approx \eta_F$ indicates the balanced configuration.

5.4. Ablation Studies on Workload and Configuration Parameters

We now investigate how the optimal A/F ratio r^* varies with key system parameters: microbatch size B , decode length distribution parameter p , and prefill length distribution parameter q .

Ablation on Batch Size B . Figure 6 compares throughput across three batch sizes ($B \in \{128, 256, 512\}$) with corresponding theoretical optimal ratios $r^* = \{7.08, 9.34, 10.31\}$. The results demonstrate that larger batch sizes achieve higher peak throughput: batching amortizes fixed overhead costs (e.g., kernel launch latency, communication setup) across more requests, thereby improving hardware utilization. Meanwhile, the optimal r^* increases moderately with B , as larger batches require more Attention instances to fully saturate the shared FFN server.

Ablation on Workload Distribution. Figure 7 examines the impact of prefill and decode length distribution. The results reveal two key findings:

(1) *The optimal r^* scales with total context length.* Both longer prefills (μ_P) and longer decode sequences (μ_D) increase the total token load in the KV cache, placing greater computational pressure on the Attention side. Consequently, more Attention instances are required to balance the shared FFN server. For example, at fixed $\mu_P = 100$, increasing μ_D from 100 to 500 raises r^* from 2.17 to 9.30; similarly, at fixed $\mu_D = 500$, increasing μ_P from 100 to 500 shifts r^* from 9.30 to 17.25.

(2) *Longer context lengths reduce peak throughput.* Con-

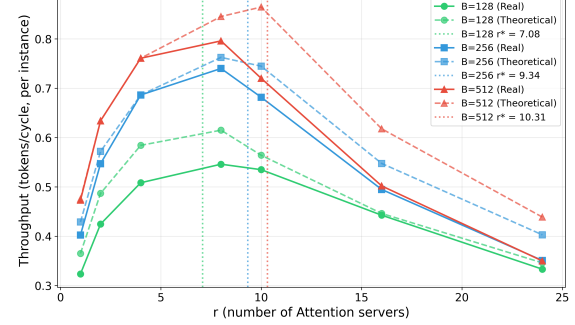


Figure 6. Impact of batch size B on per-instance throughput and optimal A/F ratio

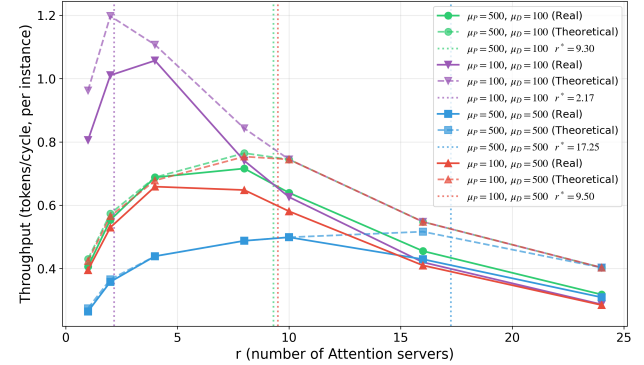


Figure 7. Impact of prefill, decode length μ_P, μ_D on per-instance throughput and optimal A/F ratio r^* . Solid lines denote simulation results; dashed lines denote theoretical predictions. Vertical dotted lines indicate the theoretical optimal r^* for each configuration.

figurations with larger $\mu_P + \mu_D$ achieve lower maximum throughput at their respective optimal r^* . This is because the per-token Attention cost grows with context length—each decode step must attend over a longer KV cache, increasing the marginal computation per output token and limiting overall efficiency.

References

Agrawal, A., Kedia, N., Panwar, A., Mohan, J., Kwatra, N., Gulavani, B., Tumanov, A., and Ramjee, R. Taming {Throughput-Latency} tradeoff in {LLM} inference with {Sarathi-Serve}. In *18th USENIX Symposium on Operating Systems Design and Implementation (OSDI 24)*, pp. 117–134, 2024.

Brown, T., Mann, B., Ryder, N., Subbiah, M., Kaplan, J. D., Dhariwal, P., Neelakantan, A., Shyam, P., Sastry, G., Askell, A., et al. Language models are few-shot learners. *Advances in neural information processing systems*, 33: 1877–1901, 2020.

Chen, L. Dissecting batching effects in GPT inference. Blog

post, May 2023. URL <https://le.qun.ch/en/blog/2023/05/13/transformer-batching/>.

Chen, Z., Bu, T., Song, C., Lu, X., Ye, Y., and Zhou, Z. A universal load balancing principle and its application to large language model serving, 2026. URL <https://arxiv.org/abs/2601.17855>.

Chowdhery, A., Narang, S., Devlin, J., Bosma, M., Mishra, G., Roberts, A., Barham, P., Chung, H. W., Sutton, C., Gehrmann, S., et al. Palm: Scaling language modeling with pathways. *Journal of Machine Learning Research*, 24(240):1–113, 2023.

Dao, T., Fu, D., Ermon, S., Rudra, A., and Ré, C. Flashattention: Fast and memory-efficient exact attention with io-awareness. *Advances in neural information processing systems*, 35:16344–16359, 2022.

Ekelund, J., Markidis, S., and Peng, I. Boosting performance of iterative applications on gpus: Kernel batching with cuda graphs. In *2025 33rd Euromicro International Conference on Parallel, Distributed, and Network-Based Processing (PDP)*, pp. 70–77. IEEE, 2025.

Kaplan, J., McCandlish, S., Henighan, T., Brown, T. B., Chess, B., Child, R., Gray, S., Radford, A., Wu, J., and Amodei, D. Scaling laws for neural language models. *arXiv preprint arXiv:2001.08361*, 2020.

Kwon, W., Li, Z., Zhuang, S., Sheng, Y., Zheng, L., Yu, C. H., Gonzalez, J., Zhang, H., and Stoica, I. Efficient memory management for large language model serving with pagedattention. In *Proceedings of the 29th symposium on operating systems principles*, pp. 611–626, 2023.

Li, Q., Zhang, B., Ye, L., Zhang, Y., Wu, W., Sun, Y., Ma, L., and Xie, Y. Flash communication: Reducing tensor parallelization bottleneck for fast large language model inference. *arXiv preprint arXiv:2412.04964*, 2024.

Lienhart, P. LLM inference series: 5. dissecting model performance. Medium, March 2024. URL <https://medium.com/@plienhar/llm-inference-series-5-dissecting-model-performance-6144aa93168f>.

Narayanan, D., Shoeybi, M., Casper, J., LeGresley, P., Patwary, M., Korthikanti, V., Vainbrand, D., Kashinkunti, P., Bernauer, J., Catanzaro, B., et al. Efficient large-scale language model training on gpu clusters using megatron-lm. In *Proceedings of the international conference for high performance computing, networking, storage and analysis*, pp. 1–15, 2021.

NVIDIA. Mastering LLM techniques: Inference optimization. NVIDIA Technical Blog, November 2023. URL <https://developer.nvidia.com/blog/mastering-llm-techniques-inference-optimization/>.

OpenAI. GPT-4 technical report. arxiv 2303.08774. *View in Article*, 2(5), 2023.

Patel, P., Choukse, E., Zhang, C., Shah, A., Goiri, I., Maleki, S., and Bianchini, R. Splitwise: Efficient generative llm inference using phase splitting. In *2024 ACM/IEEE 51st Annual International Symposium on Computer Architecture (ISCA)*, pp. 118–132. IEEE, 2024.

Pope, R., Douglas, S., Chowdhery, A., Devlin, J., Bradbury, J., Heek, J., Xiao, K., Agrawal, S., and Dean, J. Efficiently scaling transformer inference. *Proceedings of machine learning and systems*, 5:606–624, 2023.

Wang, B., Wang, B., Wan, C., Huang, G., Hu, H., Jia, H., Nie, H., Li, M., Chen, N., Chen, S., et al. Step-3 is large yet affordable: Model-system co-design for cost-effective decoding. *arXiv preprint arXiv:2507.19427*, 2025.

Wang, G., Cheng, S., Zhan, X., Li, X., Song, S., and Liu, Y. Openchat: Advancing open-source language models with mixed-quality data. *arXiv preprint arXiv:2309.11235*, 2023.

Wang, Y., Chen, Y., Li, Z., Kang, X., Tang, Z., He, X., Guo, R., Wang, X., Wang, Q., Zhou, A. C., et al. Burstgpt: A real-world workload dataset to optimize llm serving systems. *arXiv preprint arXiv:2401.17644*, 2024.

Wei, X., Moalla, S., Pascanu, R., and Gulcehre, C. Building on efficient foundations: Effective training of llms with structured feedforward layers. *Advances in Neural Information Processing Systems*, 37:4689–4717, 2024.

Yuan, Z., Shang, Y., Zhou, Y., Dong, Z., Zhou, Z., Xue, C., Wu, B., Li, Z., Gu, Q., Lee, Y. J., et al. Llm inference unveiled: Survey and roofline model insights. *arXiv preprint arXiv:2402.16363*, 2024.

Zhang, Z., Wang, Y., Wang, X., Zhao, Y., Jiang, J., Weng, Q., Shi, S., Chen, Y., and Yu, M. Janus: Disaggregating attention and experts for scalable moe inference. *arXiv preprint arXiv:2512.13525*, 2025.

Zhao, W., Ren, X., Hessel, J., Cardie, C., Choi, Y., and Deng, Y. Wildchat: 1m chatgpt interaction logs in the wild. *arXiv preprint arXiv:2405.01470*, 2024.

Zheng, L., Chiang, W.-L., Sheng, Y., Li, T., Zhuang, S., Wu, Z., Zhuang, Y., Li, Z., Lin, Z., Xing, E. P., et al. Lmsys-chat-1m: A large-scale real-world llm conversation dataset. *arXiv preprint arXiv:2309.11998*, 2023.

Zhong, Y., Liu, S., Chen, J., Hu, J., Zhu, Y., Liu, X., Jin, X., and Zhang, H. {DistServe}: Disaggregating prefill and decoding for goodput-optimized large language model serving. In *18th USENIX Symposium on Operating Systems Design and Implementation (OSDI 24)*, pp. 193–210, 2024.

Zhu, R., Jiang, Z., Jin, C., Wu, P., Stuardo, C. A., Wang, D., Zhang, X., Zhou, H., Wei, H., Cheng, Y., et al. Megascale-infer: Serving mixture-of-experts at scale with disaggregated expert parallelism. *arXiv preprint arXiv:2504.02263*, 2025.

Zuo, P., Lin, H., Deng, J., Zou, N., Yang, X., Diao, Y., Gao, W., Xu, K., Chen, Z., Lu, S., et al. Serving large language models on huawei cloudmatrix384. *arXiv preprint arXiv:2506.12708*, 2025.

A. Supplementary Materials for Section 4

A.1. Proof of Lemma 4.1

Prefill sum. By independence of $X_b(k)$ and $S'_b(k)$,

$$\mathbb{E}[s_b(k+1) \mid s_b(k)] = (1-p)s_b(k) + p\mathbb{E}[S'_b(k)] = (1-p)s_b(k) + p\mu_P.$$

Summing over $b = 1, \dots, B$ gives

$$\mathbb{E}[P_{k+1} \mid P_k] = (1-p)P_k + pB\mu_P.$$

Since $\mathbb{E}[P_0] = B\mu_P$, this recursion implies $\mathbb{E}[P_k] = B\mu_P$ for all $k \geq 0$.

Decode sum. For a request with decode length $D \sim \text{Geo}(p)$ on $\{0, 1, 2, \dots\}$, the memoryless property implies that conditional on being alive at step k , the request completes at step k with probability p and continues with probability $1-p$, independent of its current decode index $i_b(k)$. Hence, with $X_b(k) \sim \text{Bernoulli}(1-p)$,

$$i_b(k+1) = X_b(k)(i_b(k) + 1),$$

and conditioning on $i_b(k)$ yields

$$\mathbb{E}[i_b(k+1) \mid i_b(k)] = \mathbb{E}[X_b(k)](i_b(k) + 1) = (1-p)(i_b(k) + 1).$$

Summing over b gives

$$\mathbb{E}[D_{k+1} \mid D_k] = (1-p)(D_k + B).$$

By the tower property,

$$\mathbb{E}[D_{k+1}] = \mathbb{E}[\mathbb{E}[D_{k+1} \mid D_k]] = (1-p)\mathbb{E}[D_k] + (1-p)B,$$

and solving the recursion with $D_0 = 0$ yields Equation (10). \square

A.2. Proof of Proposition 4.3

By definition,

$$\begin{aligned} \bar{T}(B; N) &= \frac{1}{K(B)} \sum_{k=0}^{K(B)-1} \left(B\mu_P + B \frac{1-p}{p} (1 - (1-p)^k) \right) \\ &= B\mu_P + B \frac{1-p}{p} - B \frac{1-p}{p} \cdot \frac{1 - (1-p)^{K(B)}}{K(B)p}. \end{aligned}$$

Using $K(B) = \frac{N}{Bp}$, for large N we apply $(1-p)^{K(B)} \rightarrow 0$ and $\frac{1}{K(B)p} \rightarrow \frac{B}{N}$, yielding

$$\bar{T}(B; N) \rightarrow B \left(\mu_P + \frac{1-p}{p} \right) - \frac{1-p}{p} \cdot \frac{B^2}{N}.$$

By taking the limit on $N \rightarrow \infty$, we have the result in Proposition 4.3. \square

B. Supplementary Materials for Section 5

This appendix presents the methodology for deriving the latency model parameters $\alpha_A, \beta_A, \alpha_F, \beta_F, \alpha_C, \beta_C$ used in the main text. We demonstrate the derivation process using the DeepSeek-V3 architecture, but the methodology generalizes to other models and hardware platforms.

Note on hardware parameters. Due to confidentiality constraints, we cannot disclose the explicit Huawei Ascend 910C hardware specifications used in our experiments. Instead, we present the derivation framework using symbolic hardware parameters (summarized in Table 3), enabling practitioners to apply this methodology to their own hardware platforms. The final parameter values in Table 4 were obtained via linear regression on real execution traces over Huawei Ascend 910C.

Table 3. Hardware parameters (platform-specific, values not disclosed)

Symbol	Description
π_{peak}	Peak INT8 compute throughput (TFLOPS)
β_{HBM}	Peak HBM memory bandwidth (TB/s)
η_{mem}	Effective memory bandwidth utilization ratio
η_{compute}	Effective compute utilization ratio
β_{intra}	Intra-node interconnect bandwidth (GB/s)
β_{inter}	Inter-node network bandwidth (GB/s)
N_{cards}	Number of accelerator cards in deployment
$N_{\text{expert}/\text{card}}$	Number of experts per card

B.1. Model Configuration

We base our derivations on the DeepSeek-V3 architecture. The model has a hidden size of $H = 7168$ and uses Multi-head Latent Attention (MLA) with a compressed KV cache dimension of $(d_c + d_{\text{rope}}) = 512 + 64 = 576$. For the MoE layers, the expert intermediate dimension is $d_{\text{expert}} = 2048$, with a total of $N_{\text{expert}} = 256$ experts across the system, where each token is routed to $k = 8$ experts. We use Multi-Token Prediction (MTP) with depth 1.

B.2. MLA Attention (Memory-Bound)

During decoding, Attention computation is *memory-bound*, dominated by reading the compressed KV cache from HBM. The compute cost scales with total token load $T = \sum_{b=1}^B (s_b + i_b)$.

B.2.1. DERIVATION

Data volume per token. With KV compression dimension $(d_c + d_{\text{rope}}) = 576$ and BF16 precision (2 bytes per element):

$$V_{\text{token}} = (d_c + d_{\text{rope}}) \times 2 = 576 \times 2 = 1152 \text{ bytes.} \quad (24)$$

Effective HBM bandwidth. Accounting for non-coalesced memory access patterns, cache effects, and memory controller overhead, the effective bandwidth is:

$$\beta_{\text{eff}} = \beta_{\text{HBM}} \times \eta_{\text{mem}}. \quad (25)$$

Time per token (slope). The per-token memory access time gives the slope parameter:

$$\alpha_A = \frac{V_{\text{token}}}{\beta_{\text{eff}}} = \frac{(d_c + d_{\text{rope}}) \times 2}{\beta_{\text{HBM}} \times \eta_{\text{mem}}}. \quad (26)$$

Fixed overhead (intercept). The intercept β_A captures the other projections in the attention block, including Query/Key/Value/Output projections in memory-bound status as well as vector operations such as RMSNorm or RoPE. This parameter is best determined empirically via profiling or linear regression on execution traces.

B.3. MoE FFN (Compute-Bound)

The FFN computation is *compute-bound* when batch size is sufficiently large. Let B_e denote the batch size per expert.

B.3.1. DERIVATION

FLOPs per expert. For SwiGLU activation with 3 weight matrices (quantized gate, up, down projections):

$$\text{FLOPs per expert} = 6 \times H \times d_{\text{expert}} \times B_e = 6 \times 7168 \times 2048 \times B_e \approx 8.81 \times 10^7 \times B_e. \quad (27)$$

Effective compute throughput. For MoE workloads with dynamic routing and load imbalance, the effective throughput is:

$$\pi_{\text{eff}} = \pi_{\text{peak}} \times \eta_{\text{compute}}. \quad (28)$$

Compute time per expert.

$$t_{\text{expert}}(B_e) = \frac{6 \times H \times d_{\text{expert}} \times B_e}{\pi_{\text{eff}}} = \frac{6 \times H \times d_{\text{expert}}}{\pi_{\text{peak}} \times \eta_{\text{compute}}} \cdot B_e. \quad (29)$$

Total FFN time per card. With $N_{\text{expert/card}}$ experts per card:

$$t_{\text{FFN,card}}(B_e) = N_{\text{expert/card}} \times t_{\text{expert}}(B_e) + \beta_{\text{overhead}}. \quad (30)$$

Batch size mapping. The relationship between global batch B_F and batch per expert B_e :

$$B_e = \frac{B_F \times k \times (1 + \text{MTP depth})}{N_{\text{expert}}} = \frac{B_F \times 8 \times 2}{256} = \frac{B_F}{16}. \quad (31)$$

Express in terms of global batch. Substituting the batch size mapping, the FFN latency takes the form:

$$t_F(B_F) = \alpha_F \cdot B_F + \beta_F, \quad (32)$$

where:

$$\alpha_F = \frac{N_{\text{expert/card}} \times 6 \times H \times d_{\text{expert}}}{\pi_{\text{peak}} \times \eta_{\text{compute}}} \times \frac{k \times (1 + \text{MTP depth})}{N_{\text{expert}}}. \quad (33)$$

B.4. Communication

Communication involves transferring activations between Attention and FFN instances via high-speed interconnects.

B.4.1. DERIVATION

Data volume per batch. For a batch of B_e tokens routed to experts, the activation transfer includes input (factor of 1 with INT8 format) and output (factor of 2 with BF16 format) tokens:

$$V_{\text{comm}}(B_e) = 3 \times H \times B_e = 3 \times 7168 \times B_e = 21504 \times B_e \text{ bytes.} \quad (34)$$

Effective network bandwidth. For the AFD topology spanning both intra-node and inter-node communication, the effective aggregated bandwidth depends on the network topology and routing:

$$\beta_{\text{net}} = f(\beta_{\text{intra}}, \beta_{\text{inter}}, \text{topology}), \quad (35)$$

where the function f depends on the specific deployment configuration.

Transfer time.

$$t_{\text{comm}}(B_e) = \frac{N_{\text{expert/card}} V_{\text{comm}}(B_e)}{\beta_{\text{net}}} + \beta_C = \frac{3 \times H}{\beta_{\text{net}}} \cdot B_e + \beta_C. \quad (36)$$

Convert to per-token formulation. With batch size mapping $B_e = B_F/16$, the communication latency becomes:

$$t_C(B) = \alpha_C \cdot B + \beta_C, \quad (37)$$

where:

$$\alpha_C = N_{\text{expert/card}} \times \frac{3 \times H}{\beta_{\text{net}}} \times \frac{k \times (1 + \text{MTP depth})}{N_{\text{expert}}}. \quad (38)$$

B.5. Summary

The derivations above provide a general framework for computing latency parameters from hardware specifications and model architecture. The key relationships are:

- **Attention (memory-bound):** $\alpha_A \propto \frac{d_c + d_{\text{rope}}}{\beta_{\text{HBM}} \times \eta_{\text{mem}}}$

- **FFN (compute-bound):** $\alpha_F \propto \frac{H \times d_{\text{expert}}}{\pi_{\text{peak}} \times \eta_{\text{compute}}}$

- **Communication:** $\alpha_C \propto \frac{H}{\beta_{\text{net}}}$

Table 4 presents the parameter values used in our experiments. These values were obtained via linear regression on real execution traces collected from Huawei Ascend 910C NPUs, which provides empirical validation of the linear latency models while accounting for system-level effects not captured in first-principles analysis.

Table 4. Latency parameters obtained via linear regression on execution traces (Huawei Ascend 910C)

Equation	Symbol	Value	Unit
Eq. (2)	α_A	1.65×10^{-3}	cycles/token
	β_A	50	cycles
Eq. (3)	α_F	0.083	cycles/request
	β_F	100	cycles
Eq. (4)	α_C	0.022	cycles/token
	β_C	20	cycles

We visualize the derived latency models in Figure 8, which illustrates how Attention, FFN, and communication latencies scale with their respective input sizes under the parameters in Table 4.

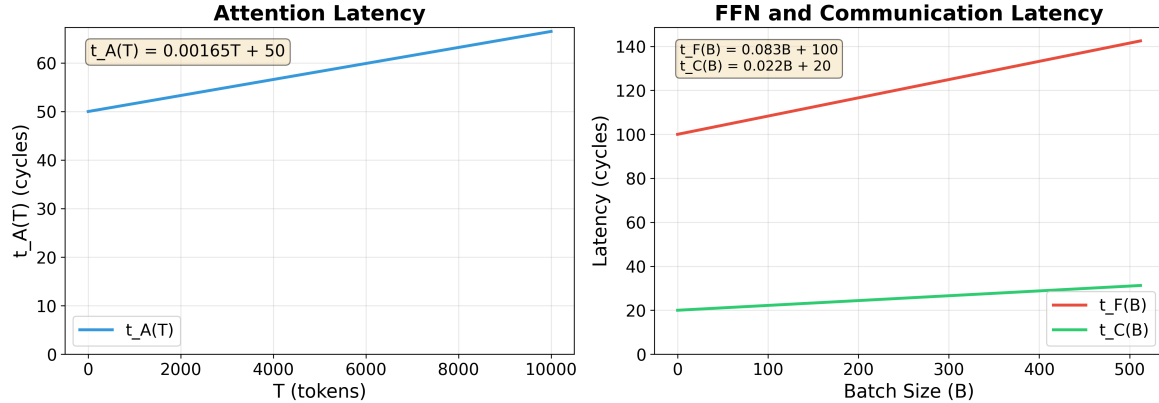


Figure 8. Visualization of the latency models. Left: Attention latency $t_A(T)$ scales linearly with total token load T . Right: FFN latency $t_F(B)$ and communication latency $t_C(B)$ as functions of batch size B .